ACCSCIENCE PUBLISHING

International Journal of Bioprinting

RESEARCH ARTICLE

Bioprinting and *in vitro* characterization of alginate–gelatin constructs incorporating human umbilical vein endothelial cells for potential cardiac tissue engineering

Farinaz Ketabat[1], Reza Gharraei[1], Alex Guinle[1,2], Nicole J. Sylvain[3], Michael E. Kelly[1,3], Ildiko Badea[4]*, and Xiongbiao Chen[1,5]*

[1]Division of Biomedical Engineering, Department of Mechanical Engineering, College of Engineering, University of Saskatchewan, Saskatoon, Saskatchewan, Canada

[2]Catholic Institute of Arts and Crafts Bretagne Campus, Vannes, Bretagne, France

[3]Department of Surgery, College of Medicine, University of Saskatchewan, Saskatoon, Saskatchewan, Canada.

[4]College of Pharmacy and Nutrition, University of Saskatchewan, Saskatoon, Saskatchewan, Canada

[5]Department of Mechanical Engineering, College of Engineering, University of Saskatchewan, Saskatoon, Saskatchewan, Canada

(This article belongs to the *Special Issue: Three-Dimensional (3D) Bioprinting for Tissue Engineering and Food Printing*)

***Corresponding authors:**
Ildiko Badea
(ildiko.badea@usask.ca)

Xiongbiao Chen
(xbc719@mail.usask.ca)

Citation: Ketabat F, Gharraei R, Guinle A, *et al.* Bioprinting and *in vitro* characterization of alginate–gelatin constructs incorporating human umbilical vein endothelial cells for potential cardiac tissue engineering. *Int J Bioprint.* 2025;11(5):385-407. doi: 10.36922/IJB025280280

Received: July 10, 2025
1st revised: August 11, 2025
2nd revised: August 26, 2025
Accepted: August 28, 2025
Published online: August 28, 2025

Abstract

Three-dimensional (3D) bioprinting offers transformative potential for cardiac tissue engineering by enabling the fabrication of cell-laden constructs. However, key challenges remain, including maintaining cell viability within bioprinted constructs and understanding how embedded cells affect their physical and mechanical properties. This study addresses these challenges by incorporating human umbilical vein endothelial cells (HUVECs) into alginate–gelatin hydrogels and evaluating their impact on mechanical, physical, and rheological properties. Bioinks or hydrogels were prepared with or without HUVECs, and their rheological properties were assessed. Computational fluid dynamics (CFD) simulation was employed to determine the appropriate bioprinting pressure while minimizing cell damage. Constructs were designed and 3D-printed with an angular pattern to replicate the orientation of cardiac myofibrils and were characterized over a 21-day period for viscoelasticity, elastic modulus, swelling, mass loss, morphology, and cell viability. The incorporation of cells increased the storage and loss moduli of the bioink, demonstrating shear-thinning behavior as described by the Cross model. CFD simulation combined with preliminary cell viability assays identified 25 kPa as a suitable 3D-printing pressure, effectively preserving cell viability. Both cell-free and cell-laden constructs exhibited viscoelastic properties; however, cell-laden constructs displayed a lower elastic modulus under linear compression, reduced swelling, and greater mass retention. High cell viability was observed immediately post-bioprinting and was maintained for more than 1 week. These findings provide a framework for developing structurally robust, cell-laden constructs with enhanced functional fidelity, supporting their application in cardiac tissue engineering.

Keywords: Cell viability; Computational fluid dynamics modeling; Physical properties; Rheology; Viscoelastic behavior

1. Introduction

Heart disease remains one of the leading causes of death worldwide, largely due to the limited regenerative capacity of the adult heart.[1–3] In many cases, heart disease leads to compromised ventricular function, including impaired filling and/or ejection of blood, resulting in heart failure (HF), a common end-stage manifestation of structural and functional cardiac disorders.[4] While heart transplantation remains the gold standard therapy for selected HF patients, offering excellent post-transplant survival, its full potential is constrained by several complications. These include immunological rejection, heightened susceptibility to infections, medication-related issues, the complex ischemic milieu, and the persistent traditional risk factors of coronary disease.[5] Consequently, regenerative therapeutic strategies have been developed to repair or replace damaged cardiac tissue.[6] However, both cell-free and cell-based approaches face limitations, including poor delivery and retention as well as limited therapeutic efficacy,[6] highlighting the need for more advanced regenerative strategies.

Cardiac tissue engineering (CTE) is a promising approach for developing functional cardiac tissue, either for *in vivo* transplantation aimed at regenerative repair or for creating *in vitro* models to study disease mechanisms and facilitate drug discovery.[7,8] Despite its promise, the success of conventional CTE depends on meeting several critical requirements that remain only partially addressed.[9] These include limited control over scaffold microarchitecture, inadequate and/or non-functional vascularization to ensure perfusion, immunogenic responses, scalability challenges, and the absence of essential cell types required for myocardial repair.[9,10]

The advancement of three-dimensional (3D) printing, one of the most widely used techniques in additive manufacturing, offers a promising avenue to overcome the aforementioned limitations.[9] More specifically, the utilization of 3D-printing to fabricate functional living constructs from biological materials—such as cells, biomaterials, and growth factors—in a spatially controlled, layer-by-layer manner is referred to as 3D-bioprinting.[9,11,12] 3D-bioprinting can be used to develop engineered tissues through two main approaches: the top-down approach, in which living cells are introduced or seeded after scaffold fabrication, and the bottom-up approach, in which living cells are incorporated during scaffold fabrication.[13,14] Although both approaches have advantages and limitations, and many recent cardiac tissue constructs employ a combination of the two, the bottom-up approach is gaining greater recognition for its effectiveness in developing vascularized tissues.[13,14]

Extrusion bioprinting is recognized as a cost-effective 3D-bioprinting technique, utilizing pneumatic- or mechanically driven fluid dispensing systems to deposit bioink with cell densities closely resembling physiological levels onto a platform.[7,15] However, excessive dispensing pressure during printing can increase shear forces acting on cells within the bioink, particularly when extruding high-viscosity bioinks or using a thin nozzle, which may reduce cell viability.[7,16] The magnitude of these shear forces is influenced by the rheological properties of the bioink and can adversely affect cell viability and proliferation, thereby impairing the biological function of the engineered tissue.[17]

Additionally, the presence of living cells can influence the physical and mechanical properties of engineered constructs.[18,19] Therefore, when bioprinting cell-laden constructs, it is important to consider: (i) applying appropriate mechanical forces during printing to minimize cell damage while ensuring proper extrudability, and (ii) characterizing their *in vitro* properties post-printing, as these may differ significantly from cell-free scaffolds. Such differences could further influence their suitability for *in vivo* applications. To the best of our knowledge, the underlying rationales for these considerations have not been thoroughly studied or reported in the literature.

Motivated by these considerations, this study aims to fabricate 3D-bioprinted constructs from alginate–gelatin hydrogel containing endothelial cells, with the goal of promoting vascularization and advancing the development of engineered cardiac tissue. The specific objectives of this study are: (i) to determine the appropriate bioprinting pressure required to maintain cell viability and apply this pressure to fabricate both cell-free scaffolds and cell-laden constructs, and (ii) to investigate the influence of incorporated cells on the physical, mechanical, and morphological properties of bioprinted constructs over time compared with cell-free scaffolds.

We first characterized the rheological behavior of the bioink composed of human umbilical vein endothelial cells (HUVECs) encapsulated in alginate–gelatin hydrogels. Rheological data were then used in computational fluid

dynamics (CFD) simulations to estimate the average velocity of the bioink during extrusion.

Based on the CFD outcomes, preliminary cell viability assays conducted over 21 days, and findings from our previous work,[20] we identified a bioprinting pressure that effectively maintained cell viability. Using this pressure, both cell-laden constructs and cell-free scaffolds (controls) were fabricated. Their mechanical and physical properties—including elastic modulus, swelling behavior, mass loss, and morphology—were evaluated over a 21-day period. Additionally, cell viability within the cell-laden constructs was assessed to confirm sustained cellular function post-bioprinting.

2. Materials and experimental methods

2.1. Hydrogel preparation

Hydrogel solutions were prepared from brown algae (A2033, Sigma-Aldrich, USA) and gelatin (Type A, gel strength approximately 300 g Bloom; G1890, Sigma-Aldrich, USA), following the method established in a previous study,[20] which demonstrated that a solution of alginate 3 wt% (Alg3) and gelatin 1 wt% (Gel1)—referred to as Alg3Gel1—was favorable for HUVECs and exhibited enhanced mechanical strength. Specifically, Gel1 was prepared by dissolving gelatin in saline solution at approximately 55°C, after which alginate powder was added to Gel1 and stirred at the same temperature until fully dissolved, forming Alg3Gel1.

In this study, Alg3Gel1 was prepared at a concentration 70% higher than that used in the previous study[20] (i.e., 4.2% instead of 3%). This allowed for subsequent dilution with the cell solution to achieve the desired final concentration of 3%. HUVECs were suspended at a density of 6×10^6 cells/mL in culture medium, following the method established in a previous study that demonstrated successful vascular network formation at this cell density.[21] The cell suspension, which comprised 30% of the bioink volume, was then combined with the hydrogel mixture to create cell-laden Alg3Gel1.

2.2. Cell culture

HUVECs (ATCC CRL-1730, American Type Culture Collection, USA) were cultured in Dulbecco's Modified Eagle Medium (SH30243.01, HyClone, Cytiva, USA) supplemented with 2% sodium hypoxanthine–aminopterin–thymidine supplement (50× stock, Gibco™, Thermo Fisher Scientific, USA), 10% fetal bovine serum (Gibco®, Invitrogen, USA), and 1% antibiotic–antimycotic (100×) containing 10,000 units/mL penicillin, 10,000 μg/mL streptomycin, and 25 μg/mL Fungizone (Thermo Fisher Scientific, USA). The cells were incubated at 37°C with 5% CO_2 and were detached using 0.25% trypsin-EDTA (Gibco®, Invitrogen, USA) once they reached approximately 80–90% confluency.

2.3. Rheological properties of the bioink

The rheological behavior of the bioinks was investigated using a rheometer. Notably, bioinks can exhibit thixotropic, viscoelastic, or shear-thinning behavior,[22] and the rheological properties of alginate-based hydrogels encapsulating HUVECs have not yet been reported in the literature.

The hydrogels were prepared according to the method described in **Section 2.1** on the day prior to testing and stored at 4°C. On the day of testing, HUVECs were counted and suspended in complete culture medium for the preparation of cell-laden bioink, while only complete culture medium was used for cell-free hydrogels. The mixtures were then gently combined to create the bioink and allowed to stand for approximately 2 h to minimize stirring effects. The hydrogels were subsequently placed onto the rheometer's lower geometry at a set temperature of 37°C using a spatula.

The flow behavior of the hydrogels and bioink was assessed using a Discovery Hybrid Rheometer HR20 (TA Instruments, USA) with a 20-mm parallel plate geometry at a shear rate range of 0.01–1000 s^{-1}. A dynamic frequency sweep test was performed at 10% strain and an angular frequency of 0.1–100 rad/s to determine the solid- and liquid-like behavior of the hydrogels and the bioink.

2.4. Determining the three-dimensional bioprinting pressure

To preserve cell viability, the appropriate 3D-printing pressure was carefully determined based on CFD simulations (to reveal process-induced forces) and preliminary cell viability assay results, as outlined below.

2.4.1. Computational fluid dynamics simulation

The bioink flow during the extrusion process was simulated using CFD. Ansys Fluent 2021-R1 finite-volume CFD software (Ansys, USA) was used to establish and solve the governing equations for bioink flow. The geometry of a 10 mL syringe connected to a luer lock GA27 tapered dispensing tip (Figure 1) was developed using SOLIDWORKS (Dassault Systèmes, France). The computational domain for fluid flow simulation was then extracted using Ansys SpaceClaim (Ansys, USA).

The bioink flow, considered incompressible, was calculated using the following equations (**Equations I–III**)[23]:

(i) Continuity:

$$\nabla \vec{U} = 0 \quad \text{(I)}$$

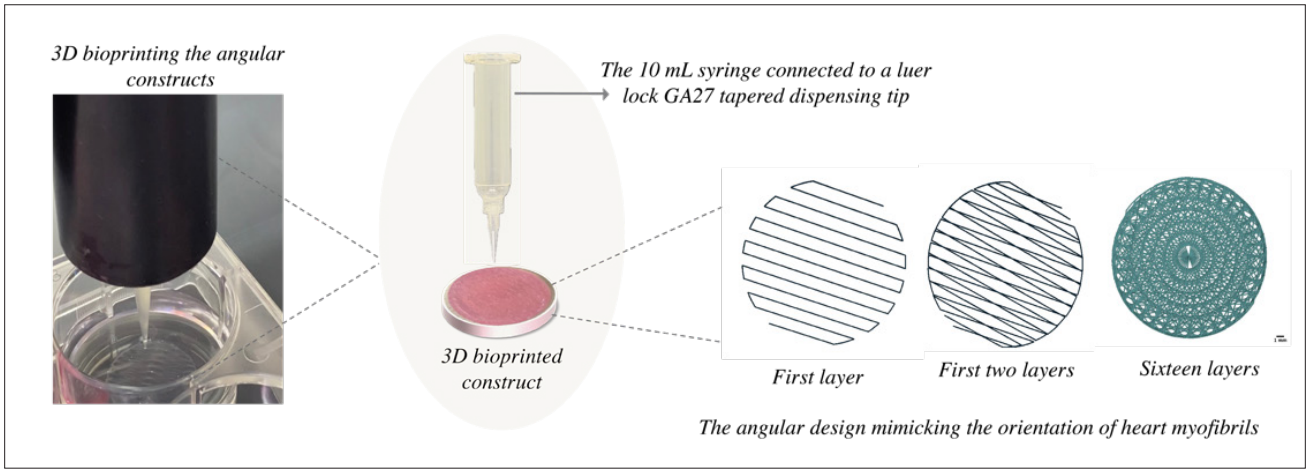

Figure 1. bioprinting of angular constructs using a 10 mL syringe equipped with a GA27 tapered dispensing tip. The construct design replicates the angular orientation of heart myofibrils. Abbreviation: 3D, three-dimensional.

(ii) Momentum:

$$\rho \frac{DU}{Dt} = \nabla.\sigma + \rho\vec{g} \quad \text{(II)}$$

$$\sigma = -pI + \tau \quad \text{(III)}$$

where $\vec{U}$ represents the fluid velocity vector, $\vec{g}$ indicates the gravitational acceleration vector, p denotes fluid pressure, ρ represents fluid density, and I is the unit tensor.[23] τ represents the shear stress tensor, which, for a Newtonian fluid, equals the shear rate tensor ($\dot{\gamma}$) multiplied by the dynamic viscosity η, according to Newton's viscosity law.[23]

$$\tau = \eta\dot{\gamma} \quad \text{(IV)}$$

For non-Newtonian fluids, the generalized form of **Equation IV** is used, where η is replaced with an apparent viscosity that varies with shear rate.[23]

The mathematical model that best fit the flow behavior data was extracted using TRIOS software (TA Instruments, USA). The computational solution of **Equations I–III**, with appropriate boundary conditions and a suitable flow behavior model (**Equation IV**), provides a detailed description of the flow inside the syringe and dispensing tip during extrusion. The boundary conditions were defined as follows: "pressure inlet" at the free surface of the bioink inside the syringe; "pressure outlet" at the environmental gauge pressure; and a "no-slip" condition on all solid walls. The computational simulations, performed using Ansys Fluent 2021-R1 software, yielded the distribution of velocity components, pressure, shear rate, and shear stress.

2.4.2. Cell viability

To evaluate the effect of printing pressure on cell viability, bioinks were extruded at 20 kPa and 30 kPa to fabricate single-layer constructs. Cell viability was assessed immediately after printing and again on the following day. In addition, 16-layer constructs were bioprinted, and cell viability was evaluated on days 1, 7, and 21 using a live/dead assay. The assay employed calcein-AM (1 µg/mL) and propidium iodide (10 µg/mL) in complete culture medium to stain live and dead cells, respectively. After 40 min of incubation at room temperature, the single-layer constructs were imaged using a BioTek Lionheart LX automated microscope (Biotek Instruments, Winooski, VT, USA), and the 16-layer constructs were imaged using a Leica TCS SPEII confocal microscope (Leica Microsystems, Wetzlar, Germany)). All live/dead assays were performed using the same protocol to ensure consistency and reproducibility across experiments.

2.5. Three-dimensional printing or bioprinting

Cylindrical constructs (20 mm × 20 mm) were designed and printed with a strand diameter of 0.15 mm and an infill distance of 1.5 mm. These parameters were selected based on a previous study, in which angular scaffolds fabricated from the Alg3Gel1 formulation (infill distance: 1.5 mm; strand diameter: 0.15 mm) exhibited the highest support

for cell viability and superior elastic modulus among the tested groups.[20] Cell-free scaffolds and cell-laden constructs were printed in 16 layers using a 27G SmoothFlow tapered tip with an inner diameter of 0.2 mm (Nordson EFD, USA) on a BioScaffolder 3.2 (Gesim, Germany). The scaffolds were printed with a gradual angular change in each layer (Figure 1), using a printing speed of 4 mm/s and a pressure of 25 kPa. The first layer was deposited at a −70° angle, with each successive layer rotated by 10°, until the final layer, which was deposited at +80° angle.

The day before printing, 6-well plates were coated with 0.1% polyethyleneimine (PEI; molecular weight 60,000; 50% w/w aqueous solution) (Thermo Fisher Scientific, USA) and incubated at 37°C. On the day of printing, the PEI solution was replaced with 50 mM calcium chloride prepared in 0.1% PEI solution. The scaffolds were printed directly into wells containing the prepared solution and left for 15 min post-printing to ensure effective crosslinking. They were then washed three times with culture medium and transferred to complete culture medium.

2.6. Rheological, mechanical, swelling, and mass retention properties of constructs

The physical properties of the printed constructs were assessed by evaluating their rheological properties, elastic modulus, swelling behavior, and mass retention percentages.

2.6.1. Mechanical and rheological properties

The elastic modulus (Young's modulus) of both cell-free and cell-laden constructs was assessed using the ElectroForce Biodynamic 5100 series (TA Instruments, USA). A compression force was applied to the printed constructs at a rate of 0.01 mm/s until they were compressed to 50% of their initial height. The stress–strain curve for each scaffold was then plotted, and the elastic modulus was calculated as the slope of the linear region.

Given that the viscoelasticity of the myocardium is crucial for cardiac function, it was essential to evaluate both the storage modulus (G') and the loss modulus (G"). Before conducting the frequency sweep test, a strain sweep was performed on the scaffolds using the HR-20 equipped with linear dynamic mechanical analysis capability. The strain sweep, conducted at an angular frequency of 1 Hz, involved an amplitude range of 1–100 μm to determine the linear region. A strain value within this range (3%) was selected for the frequency sweep test. The frequency sweep test was performed on the printed constructs at 37°C to obtain G' and G" as functions of frequency over the range of 1–16 s^{-1}. The initial strain was set to 5% of the initial height of the scaffolds.

2.6.2. Swelling and mass retention

The swelling and mass retention percentages of the constructs play an important role in regulating cell growth and function. Constructs with a high degree of swelling may promote cell attachment, while degradation that occurs neither too early nor too late provides adequate support for cell growth and proliferation.[14] Swelling and mass retention of the constructs were assessed over 21 days while being maintained in complete culture medium in an incubator at 37°C and 5% CO_2. After the constructs were printed, crosslinked, and washed three times with Dulbecco's Modified Eagle Medium, they were blotted and weighed under sterile conditions to record their initial weight (W_0). Subsequently, the constructs were maintained in complete culture medium at 37°C with 5% CO_2. At different time points (days 1, 3, 7, and 21), the constructs were removed, blotted, and weighed (W_t). The swelling percentage was then calculated using **Equation V**:

$$Swelling\ (\%) = \frac{W_t - W_0}{W_0} \times 100 \quad \text{(V)}$$

where W_0 is the initial weight of the constructs immediately after printing, and W_t is the wet weight of the constructs at different time points (days 1, 3, 7, and 21).

The same constructs were also used for the mass retention test. In this case, the constructs were lyophilized after weighing at different time points, and their dry weight was recorded (W_t). To determine the initial dry mass of the constructs, separate constructs were printed, and their average weight was designated as the initial lyophilized mass (W_0). The mass retention percentage was then calculated using **Equation VI**[24]:

$$Mass\ retention\ (\%) = 100 - \frac{W_0 - W_t}{W_0} \times 100 \quad \text{(VI)}$$

For each time point, the swelling and mass retention percentages were calculated using at least six replicates.

2.7. Field emission scanning electron microscopy

The microstructure and morphology of the printed constructs were examined using a Hitachi SU8010 field emission scanning electron microscope (FESEM) (Hitachi, Japan). After lyophilization, the constructs were sputter-coated with gold and observed under FESEM at a voltage of 3 kV and a current of 10 μA, at two different magnifications.

2.8. Statistics

All quantitative data are presented as mean ± standard deviation. Statistical analyses were performed using one-

way analysis of variance (ANOVA), followed by Tukey's post hoc test for multiple comparisons. All analyses were conducted using GraphPad Prism version 10.4.0 (GraphPad Software, USA).

3. Results

3.1. Rheological properties of the bioink

To examine the impact of incorporating cells into the Alg3Gel1 bioink and to determine appropriate 3D-printing parameters for bioprinting, the rheological behavior of cell-laden Alg3Gel1 was compared with that of Alg3Gel1 and Alg3. Figure 2 illustrates the shear stress and viscosity of the hydrogels and bioink as functions of shear rate. Figure 2A presents the relationship between shear stress and shear rate for Alg3, Alg3Gel1, and cell-laden Alg3Gel1. The non-linear relationship observed in all three samples indicates their non-Newtonian fluid behavior. The cell-laden Alg3Gel1 showed the highest shear stress across the tested shear rates, likely due to the presence of cells acting as suspended particles, thereby increasing the viscosity of the suspension compared to the base fluid.

At lower shear rates, Alg3Gel1 exhibited higher shear stress than Alg3, suggesting that the addition of Gel1 influences fluid behavior, particularly under lower-shear conditions. Figure 2B plots the viscosity against shear rate for the same three samples. All samples exhibited lower viscosities at higher shear rates—a characteristic of shear-thinning fluids. The cell-laden Alg3Gel1 displayed the highest viscosity at lower shear rates, which decreased rapidly with increasing shear rate, indicating pronounced shear-thinning behavior. While both Alg3 and Alg3Gel1 demonstrated shear-thinning properties, the addition of Gel1 consistently resulted in higher viscosities across most of the shear-rate range.

Based on the mathematical model fitting using TRIOS software, the Cross time-independent model provided the best fit for the data in Figure 2B among the array of models available. This model describes the flow behavior of shear-thinning fluids across a wide range of shear rates (**Equation VII**).

$$\frac{\eta-\eta_{\infty}}{\eta_0-\eta_{\infty}}=\frac{1}{1+k\dot{\gamma}^{n}} \quad \text{(VII)}$$

where k and n are fitting parameters, η_0 is the limiting viscosity at low shear rates, and η_∞ is the limiting viscosity at high shear rates.[25] Table 1 presents the parameters of the Cross model characterizing the flow behavior of cell-laden Alg3Gel at 37°C.

Figure 3 shows the rheological properties of the hydrogels and bioink as a function of frequency. Figure 3A depicts the storage modulus (G'), which reflects the solid-like behavior of the samples. Among all samples, the cell-laden Alg3Gel1 exhibited the highest G', indicating the most solid-like behavior. In contrast, Alg3 showed the lowest G', demonstrating the least solid-like behavior. Interestingly, while Alg3Gel1 showed the second-highest G' in its unloaded form, the presence of cells in the cell-laden Alg3Gel1 further increased its stiffness.

Figure 3B illustrates the loss modulus (G"), which reflects the liquid-like behavior of the samples. Similar to the storage modulus, the cell-laden Alg3Gel1 exhibited the highest G" among all samples, while Alg3 displayed a lower G" than the cell-laden Alg3Gel1. Alg3 also exhibited the lowest G" overall. Taken together, the cell-laden Alg3Gel1 exhibited the highest G' and G" among all samples.

Figure 3C shows the ratio of G" to G' (tan δ) for both cell-free and cell-laden hydrogels. The data indicate that the cell-laden Alg3Gel1 had a higher G" than G', suggesting more solid-like behavior in the cell-laden Alg3Gel1. In contrast, both Alg3Gel1 and Alg3 exhibited the opposite trend, with a greater loss modulus than storage modulus.

3.2. Preliminary cell viability and computational fluid dynamics modeling

In this study, the bioprinting process parameters were determined based on CFD simulations and preliminary cell viability tests. As demonstrated in our previous study,[20] printing Alg3Gel1 scaffolds at 20 kPa of pressure and 4 mm/s speed resulted in scaffolds with a high elastic modulus, high swelling percentage, minimal mass loss, excellent printability, and high cell viability, making them ideal for engineered cardiac tissue. However, incorporating cells into the bioprinting process introduces a critical challenge—potential cell damage caused by bioprinting process-induced forces.

3.2.1. Preliminary cell viability analysis

A preliminary cell viability assay was employed to assess the effect of 3D-bioprinting pressure on cell viability.

Table 1. Parameters of the Cross model used to describe the flow behavior of the bioink at 37°C

Fluid	η_0 (Pa·s)	η_∞ (Pa·s)	k (s)	n
Cell-laden Alg3Gel1	110.34	9.16×10^{-16}	1.01	0.62

Notes: k and n are fitting parameters, η_0 is the limiting viscosity at low shear rates, and η_∞ is the limiting viscosity at high shear rates.

Abbreviation: Alg3Gel1, alginate 3 wt%–gelatin 1 wt%.

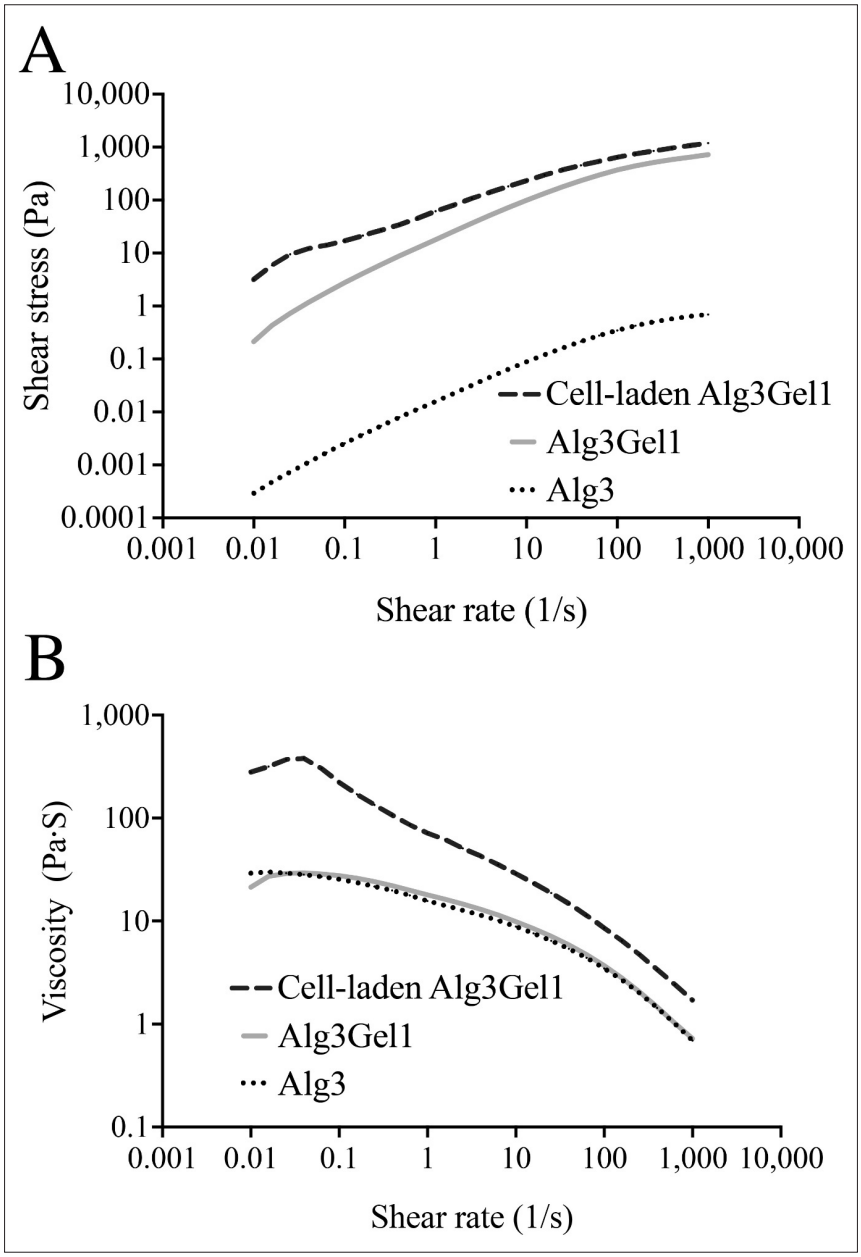

Figure 2. Rheological behavior of the hydrogels as a function of shear rate: (A) Shear stress vs. shear rate and (B) viscosity vs. shear rate. Abbreviations: Alg3, alginate 3 wt%; Alg3Gel1, alginate 3 wt%–gelatin 1 wt%.

In this study, the bioink was 3D-bioprinted into a single layer at pressures of 20 and 30 kPa. The theoretical fiber thickness was 0.15 mm, and the infill distance was 1.5 mm. For the 20 kPa pressure, the fiber thickness and infill distances were adjusted in terms of printability, mechanical properties, and the ability to support high cell viability, as determined in our previous study on cell-free scaffolds.[20]

Following the live/dead assay, all constructs exhibited high cell viability both immediately after bioprinting and on the following day. No noticeable differences in immediate post-printing viability were observed between constructs printed at 20 and 30 kPa. This is likely due to the delayed onset of mechanical stress-induced cellular responses, which typically require at least overnight incubation before detection via viability measurements.

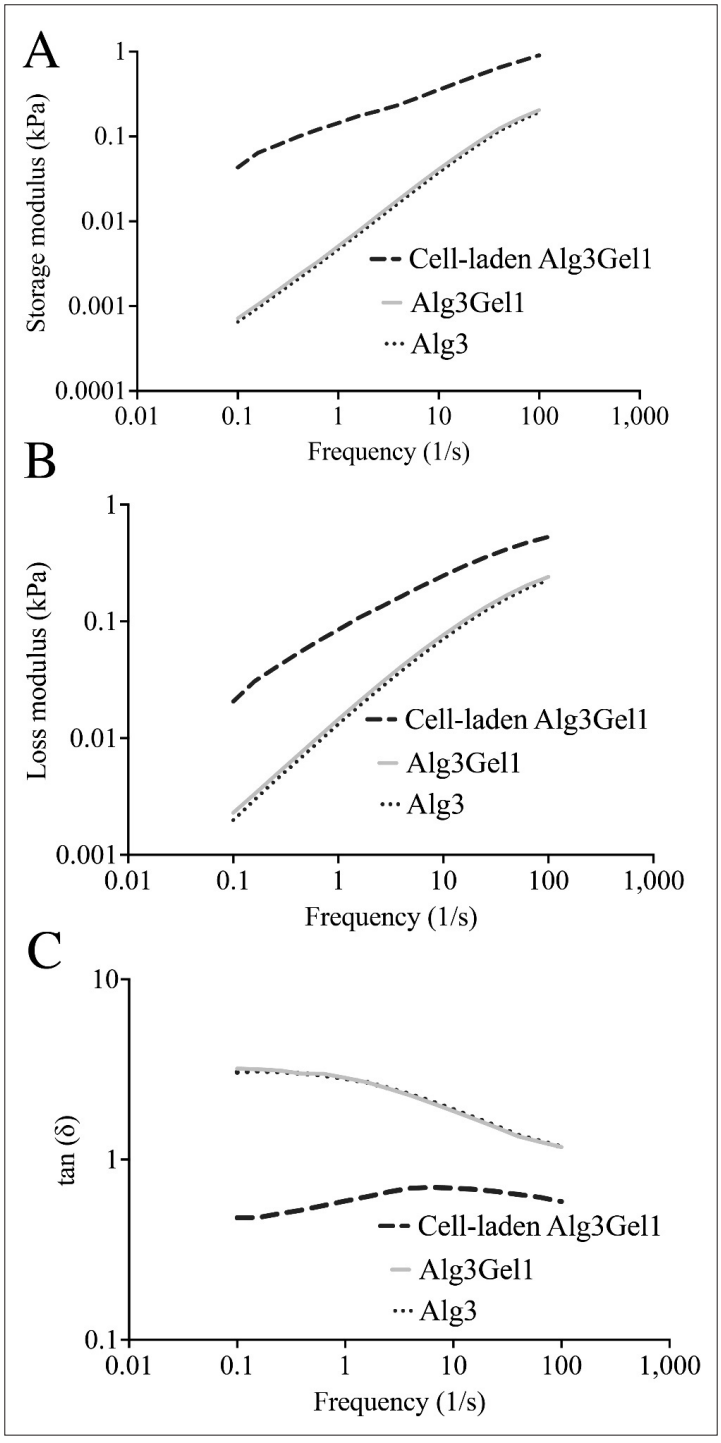

Figure 3. Frequency-dependent rheological properties of hydrogels and bioink: (A) Storage modulus (kPa) of cell-laden Alg3Gel1, Alg3Gel1 without cells, and Alg3 across a range of frequencies, (B) loss modulus (kPa) of the same groups, illustrating the viscous response under varying frequencies, and (C) tan δ (ratio of loss modulus to storage modulus) as a function of frequency. Abbreviations: Alg3, alginate 3 wt%; Alg3Gel1, alginate 3 wt%–gelatin 1 wt%.

The only noticeable difference was that a pressure of 30 kPa resulted in fibers with a greater thickness of approximately 0.6 mm, compared to the layer printed at 20 kPa, which had an approximate thickness of 0.3 mm (Figure S1). However, when 16-layer constructs were 3D-bioprinted using pressures of 20 and 30 kPa, significant differences were observed (Figure S2). On the first day after 3D-bioprinting, constructs printed at 20 kPa exhibited high cell viability. By day 21, the total cell count—including both viable and non-viable cells—significantly decreased for constructs printed at 30 kPa. Preliminary visual observations revealed that 3D-bioprinted constructs printed at 20 kPa exhibited fibers that appeared narrower compared to both cell-free fibers printed under the same pressure and cell–laden hydrogels printed at 30 kPa. These narrower fibers subsequently disintegrated after 21 days.

3.2.2. Computational fluid dynamics modeling

The numerical solution of the governing equations, along with specified boundary conditions, provides the distribution of velocity and pressure within the bioink as it flows through the syringe and nozzle. Additionally, the distribution of shear stress is calculated based on velocity gradients and the apparent viscosity distribution. Figure 4 illustrates the distribution of shear stress inside the syringe and printing nozzle. Simulations with different printing pressures revealed varying shear stress values near the nozzle outlet. Comparing the shear stress values for each printing pressure indicates an increase in shear stress with higher printing pressures. Table 2 lists the maximum shear stress values inside the nozzle for different printing pressures. Given the direct relationship between cell damage and shear stress, the CFD results suggest that the lowest applicable pressure capable of producing a stable fiber is the appropriate choice for printing.

The average velocity of bioink at the nozzle outlet can be calculated by area-weighted averaging of the normal component of velocity at the outlet. Applying different values of pressure boundary conditions on the bioink surface inside the syringe results in corresponding differences in the average velocity at the nozzle outlet. The average outlet velocity of extruded cell-laden Alg3Gel1 at a printing speed of 4 mm/s for different printing pressures, ranging from 20 to 40 kPa, is shown in Figure 5.

Given that the printing speed was set to 4 mm/s, only a pressure of 25 kPa resulted in an average outlet velocity of 4.26 mm/s (deposition speed), which is close to the printing speed. Minimizing the difference between deposition and printing speeds in extrusion bioprinting facilitates smooth and uniform bioink flow during extrusion from the nozzle, thereby improving printability. If the printing speed exceeds the deposition speed, the strand will be stretched,

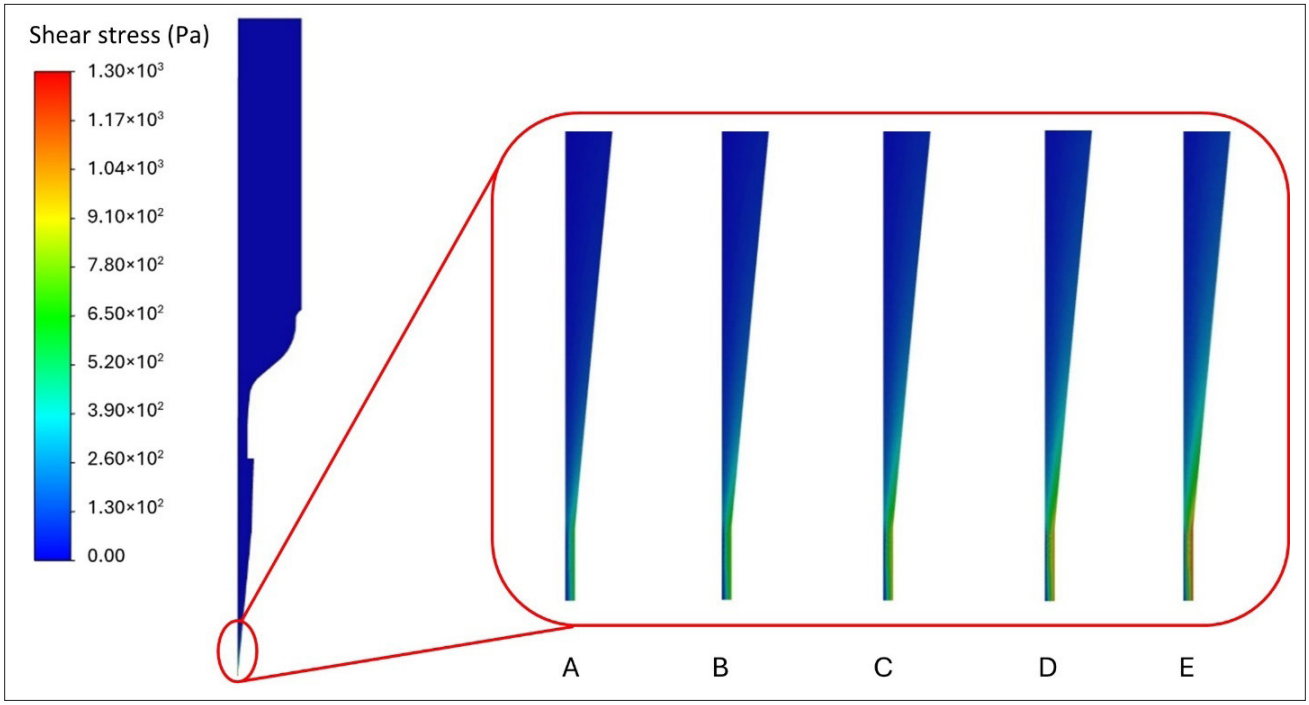

Figure 4. Distribution of shear stress inside the syringe and printing nozzle; magnified view of shear stress distribution near the nozzle outlet at printing pressures of (A) 20 kPa, (B) 25 kPa, (C) 30 kPa, (D) 35kPa, and (E) 40 kPa.

Table 2. Maximum shear stress values within the nozzle at different printing pressures

Printing pressure (kPa)	Maximum shear stress
20	685.37
25	839.76
30	992.34
35	1143.58
40	1293.79

causing cells to experience extensional stress that may damage their membranes.

Although compressive forces from hydrostatic pressure are minor, cell membranes may twist and stretch, potentially leading to cell damage if shear forces exceed physiological thresholds. Cells are particularly vulnerable when passing through the needle's constrictive region, where they are directly stretched and exposed to extensional stress.[26] A printing pressure of 20 kPa produces the minimum shear stress among the aforementioned cases. However, strands printed at 20 kPa are prone to lower printability and reduced cell viability due to the difference between dispensing and printing speeds. Therefore, a pressure of 25 kPa appears more suitable for bioprinting cell-laden Alg3Gel1 hydrogel constructs, ensuring adequate structural integrity and longevity. Consequently, we proceeded with the rest of the experiments using this pressure.

3.3. Mechanical, rheological, swelling, and mass retention properties of constructs

3.3.1. Mechanical and rheological properties

The elastic modulus of both cell-free and cell-laden Alg3Gel1 constructs is shown in Figure 6. The elastic modulus of cell-free scaffolds was measured as 9.24 ± 1.65 kPa, 10.08 ± 2.62 kPa, 11.27 ± 1.72 kPa, 7.20 ± 1.74 kPa, and 6.17 ± 1.27 kPa on days 0, 1, 3, 7, and 21, respectively. Similarly, the elastic modulus of cell-laden constructs was measured as 3.50 ± 0.71 kPa, 11.16 ± 2.43 kPa, 4.88 ± 1.37 kPa, 5.18 ± 2.42 kPa, and 4.65 ± 1.50 kPa on days 0, 1, 3, 7, and 21, respectively.

The elastic modulus of cell-free scaffolds showed an increasing trend from day 0 to day 3, followed by a decrease from day 7 to day 21. Day 3 exhibited the highest elastic modulus among all observed time points for cell-free scaffolds. Similarly, the elastic modulus of cell-laden constructs showed an initial increase from day 0 to day 1, followed by a decrease from day 1 to day 3. There was a slight increase on day 7, followed by a slight decrease on day 21. Although the elastic modulus values for cell-

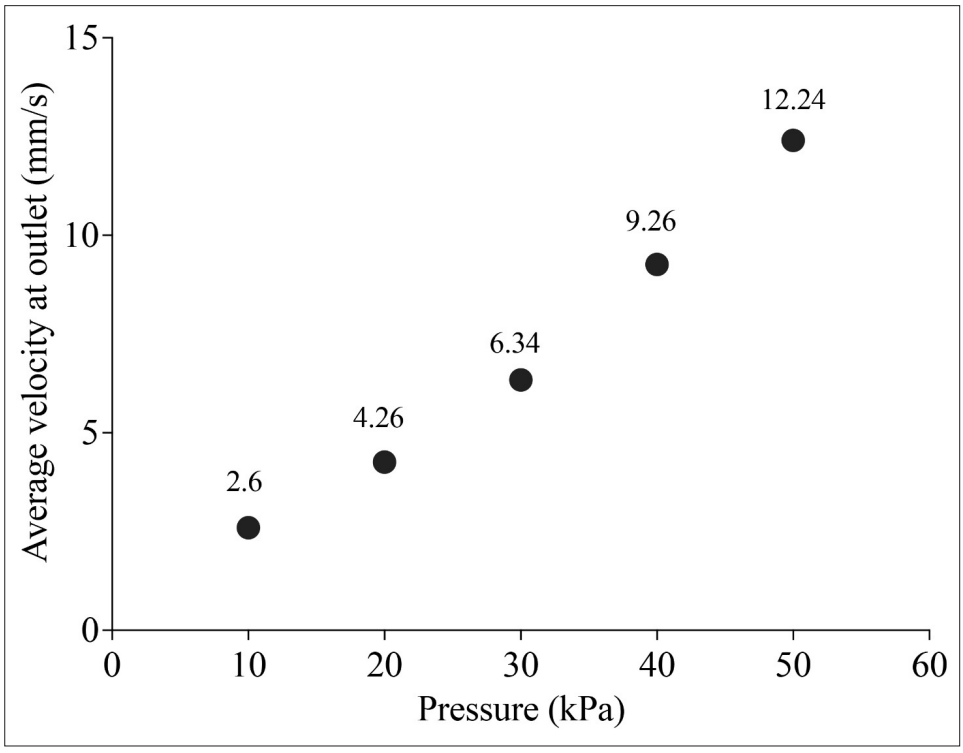

Figure 5. Calculated average outlet velocity at different printing pressures using the Cross model.

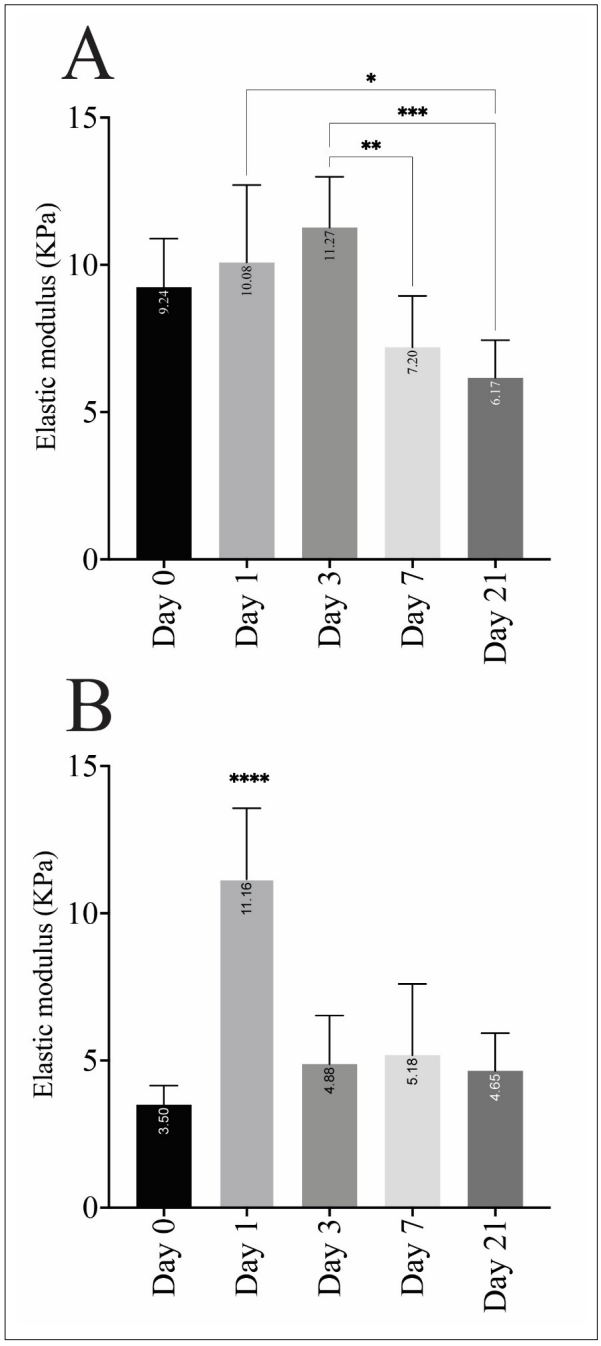

Figure 6. Elastic modulus of (A) three-dimensional-printed scaffolds and (B) cell-laden constructs. Statistical comparisons were performed using *one-way ANOVA* followed by Tukey's *post hoc test*. Significance thresholds: *$p < 0.05$, **$p < 0.01$, *** $p < 0.001$, ****$p < 0.0001$.

laden constructs are generally lower than those of cell-free scaffolds across most time points, they are significantly lower only on day 0 ($p = 0.000110$) and day 3 ($p < 0.000001$) compared to the cell-free scaffolds.

The storage (G') and loss (G") moduli versus frequency for both cell-free and cell-laden constructs are presented in Figure 7A and B, respectively. The G' of cell-free scaffolds was 3.94 kPa at 1 Hz and decreased to 2.37 kPa at 16 Hz. Concurrently, the G" was 0.83 kPa at 1 Hz and increased to 7.70 kPa at 16 Hz. For cell-laden constructs, the G' was 0.1 kPa at 1 Hz and decreased to 0.06 kPa at 16 Hz, while the G" was 0.04 kPa at 1 Hz and increased to 0.33

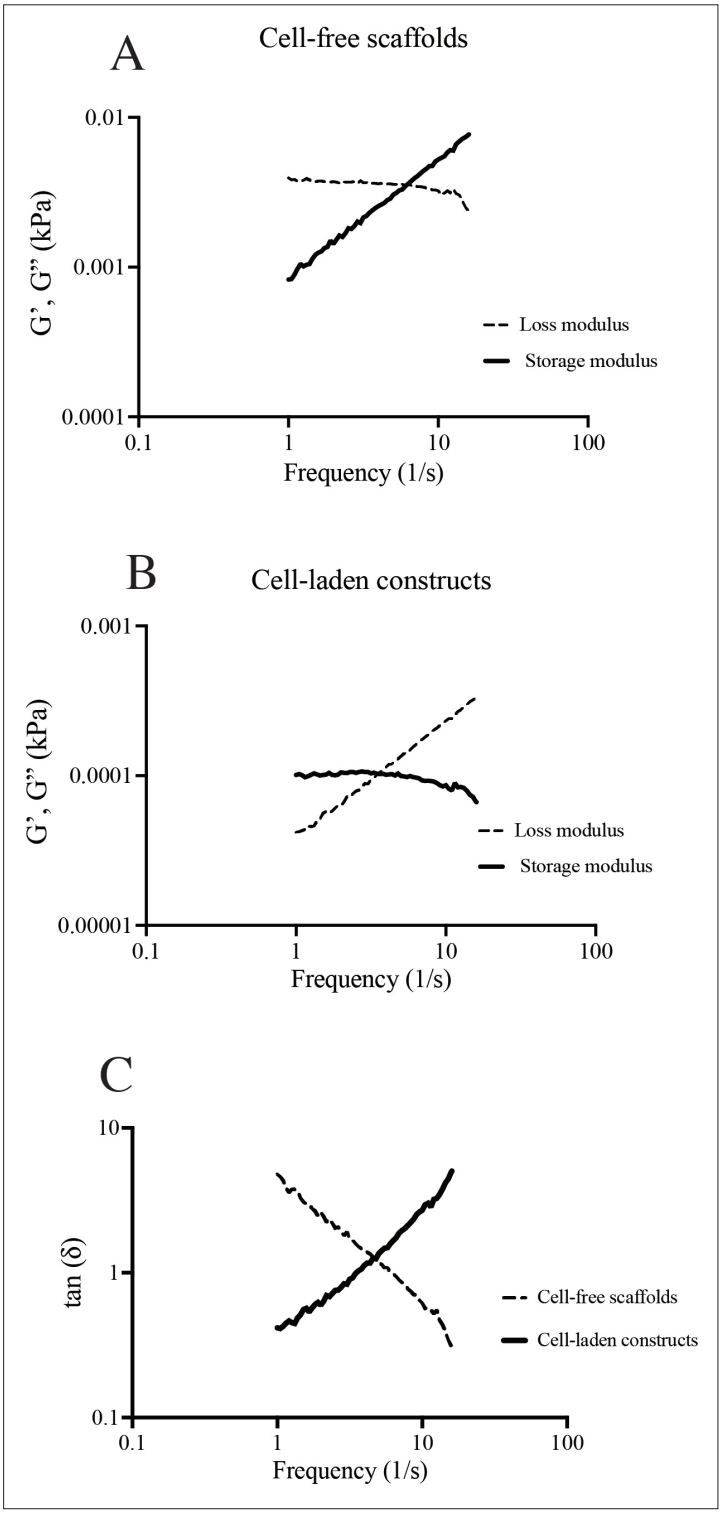

Figure 7. Viscoelastic behavior of three-dimensional-printed scaffolds and constructs: (A) Storage and loss moduli of cell-free scaffolds, (B) storage and loss moduli of Cell-laden constructs, and (C) tan δ of both cell-free scaffolds and cell-laden constructs.

kPa at 16 Hz. These findings indicate that both cell-free and cell-laden constructs exhibited viscoelastic behavior. However, the cell-laden constructs demonstrated less solid-like and more liquid-like behavior compared to the cell-free scaffolds. Figure 7C shows the damping factor (tan δ) for both cell-free and cell-laden constructs. For cell-laden constructs, tan δ was less than 1 at low frequencies, indicating more solid-like behavior, and exceeded 1 at higher frequencies, suggesting more liquid-like behavior. In contrast, cell-free scaffolds displayed the opposite trend, with tan δ greater than 1 at low frequencies and less than 1 at higher frequencies.

3.3.2. Swelling and mass retention percentages

The swelling and mass retention percentages of the cell-free and cell-laden constructs following incubation in complete culture medium over 21 days are shown in Figure 8**.** The swelling percentage of cell-free scaffolds was measured as 76.78, 80.25, 60.49, and 80.42% on days 1, 3, 7, and 21, respectively (Figure 8A). These scaffolds maintained a consistent swelling percentage throughout the experimental period, except on day 7, where they exhibited a statistically lower swelling percentage compared to days 3 and 21 ($p < 0.05$). Similarly, the cell-laden constructs maintained a consistent swelling percentage throughout the experiment, with a slight increase observed on day 21 post-printing, reaching statistical significance compared to day 7 ($p < 0.05$). The swelling percentage of cell-laden constructs was 62.33, 60.97, 53.45, and 72.98% on days 1, 3, 7, and 21, respectively (Figure 8C). While the swelling percentage of cell-free scaffolds was higher compared to that of the cell-laden constructs at each time point, no statistical difference was observed between them on any respective day, as determined by a one-way ANOVA with Tukey's post hoc multiple comparisons test.

The mass retention percentages of cell-free scaffolds (Figure 8B) demonstrated that these scaffolds retained more than 70% of their initial mass throughout the experimental period. Specifically, on day 1, the mass retention was 72.04%, followed by a significant increase ($p < 0.01$) to 83.95% on day 3. Conversely, a significant decrease in mass retention percentage was observed on day 7 ($p < 0.01$), decreasing to 73.62%. Interestingly, on day 21, a significant gain in mass ($p < 0.05$) was observed, reaching 83.82%. These findings highlight the dynamic nature of mass changes in the cell-free scaffolds over the experimental period. In contrast, the cell-laden constructs consistently exhibited nearly 100% mass retention over the 21-day period (Figure 8D). Overall, the mass retention percentage of cell-laden constructs was higher than that of the cell-free scaffolds at each time point ($p < 0.0001$), as determined by a one-way ANOVA with Tukey's post hoc multiple comparisons test.

3.4. Field emission scanning electron microscopy analysis

To examine the morphological changes of the printed structures over time, FESEM was employed to capture images of the lyophilized cell-free scaffolds (Figure 9) and cell-laden constructs (Figure 10).

The FESEM images of the cell-free scaffolds displayed signs of mass loss, which were noticeable from day 1. These changes became more pronounced by day 7 and peaked on day 21, providing visual insights into the progressive mass loss of the scaffolds over the 21-day period. The images of the cell-laden constructs revealed a more pronounced mass loss from day 1 to day 7 compared to the cell-free scaffolds. Surprisingly, by day 21, the cell-laden constructs exhibited a more uniform structure while maintaining their angular and hierarchical characteristics.

3.5. Cell viability analysis

To evaluate the distribution and viability of the 3D-bioprinted cells within the constructs, a live/dead assay was conducted over a 21-day period (Figure 11). The findings revealed that the majority of the cells were viable post-printing (Figure 9A–C). During the first 3 days post-printing, a notable increase in the density of viable cells was observed, along with the detection of a small population of dead cells. From day 7 to day 21, both the viable and dead cell populations decreased. These findings suggest that HUVECs tolerated 3D-printing well, with only minor adverse effects.

4. Discussion

Understanding the rheology and flow behavior of inks, particularly bioinks, before proceeding with extrusion 3D-printing is essential to ensure the fabrication of precise 3D-bioprinted constructs with high cell viability. Higher ink viscosity improves the mechanical properties of the ink, potentially resulting in improved printing resolution and greater printing fidelity.[27,28] While a controlled applied load on living cells may promote growth, locomotion, and differentiation, increasing the applied pressure can elevate nozzle–wall shear stress, leading to clogging of the printing nozzle, which could negatively affect cell viability and cell phenotype.[29,30] Bioprinting may reduce cell viability to below 60%, depending on the cell type.[31] Here, a primary challenge was to determine the appropriate printing pressure for fabricating a cell-laden construct using a bottom-up approach, ensuring high cell viability while maintaining printing parameters comparable to those used in previously fabricated structures with the top-

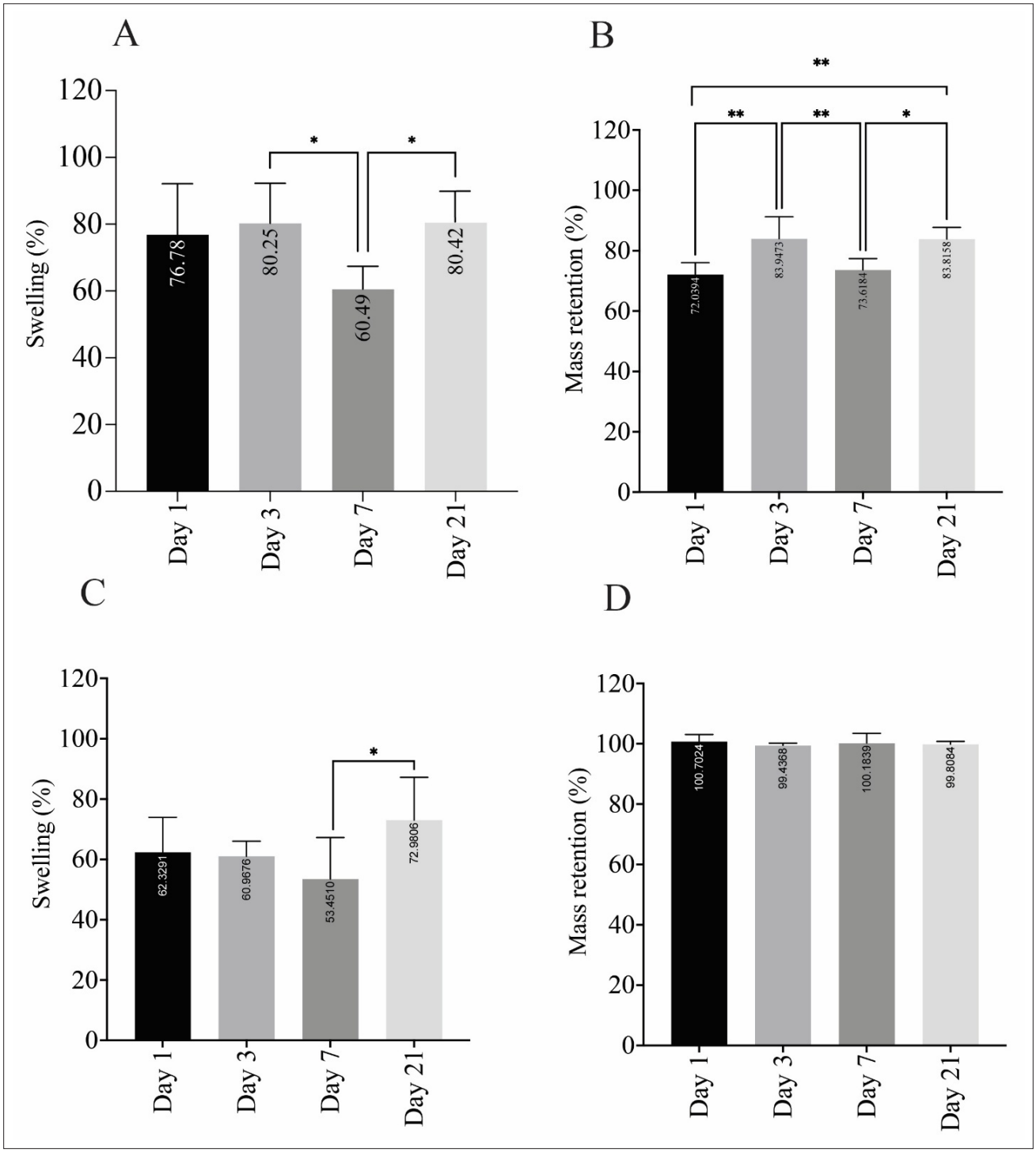

Figure 8. Swelling and mass retention percentage for cell-free scaffolds and cell-laden constructs: (A) the swelling percentage of cell-free scaffolds, (B) the mass retention percentage of cell-free scaffolds, (C) the swelling percentage of cell-laden constructs, and (D) the mass retention percentage of cell-laden constructs. The data in each graph were compared within the same graph using one-way ANOVA followed by Tukey's post hoc test. Significance thresholds: *$p < 0.05$, **$p < 0.01$.

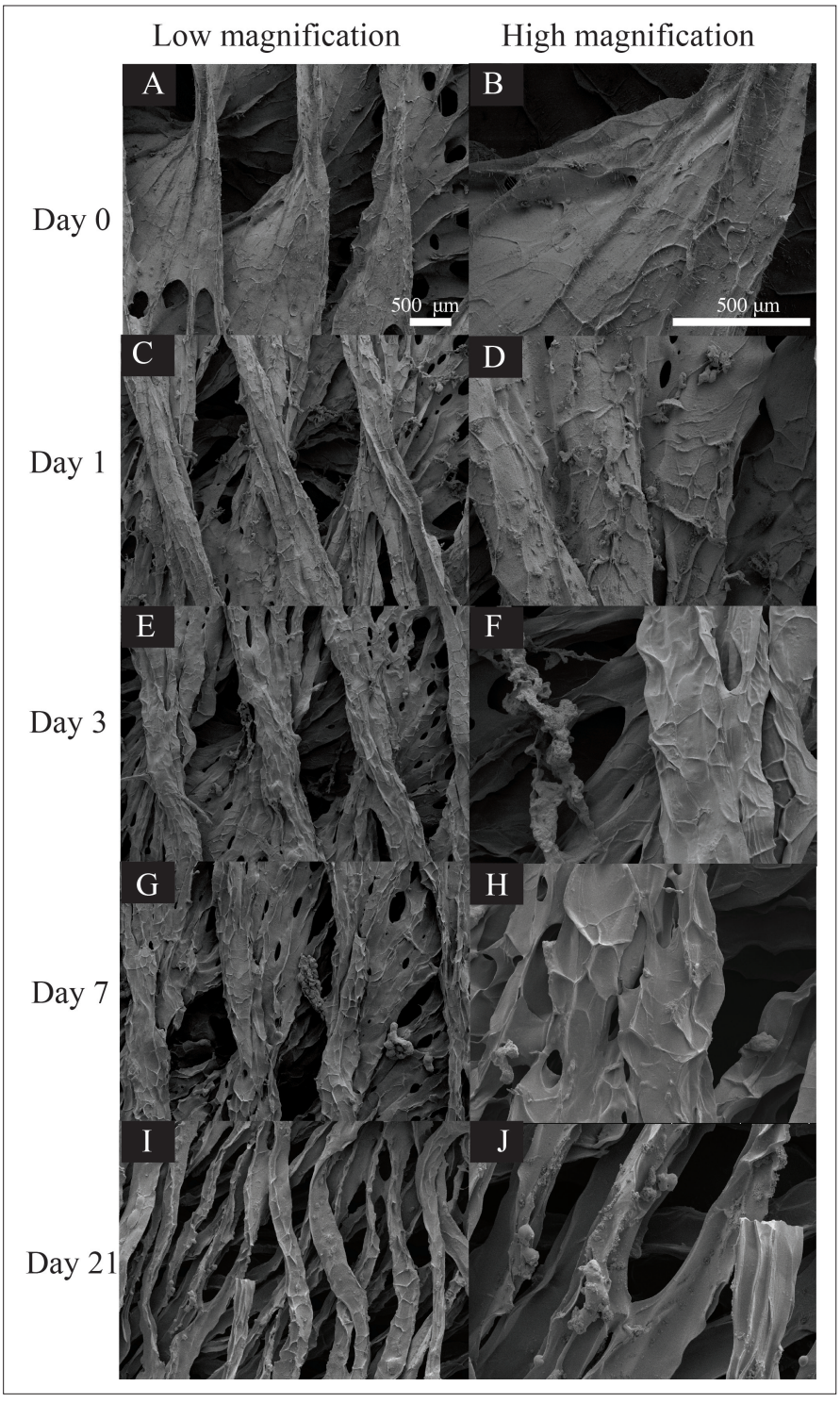

Figure 9. Field emission scanning electron microscopy images of lyophilized cell-free scaffolds at different time points. Low magnification images on (A) day 0, (C) day 1, (E) day 3, (G) day 7, and (I) day 21 (scale bar: 500 μm; magnification: 30×), and corresponding higher-magnification images on (B) day 0, (D) day 1, (F) day 3, (H) day 7, and (J) day 21 (scale bar: 500 μm; magnification: 100×).

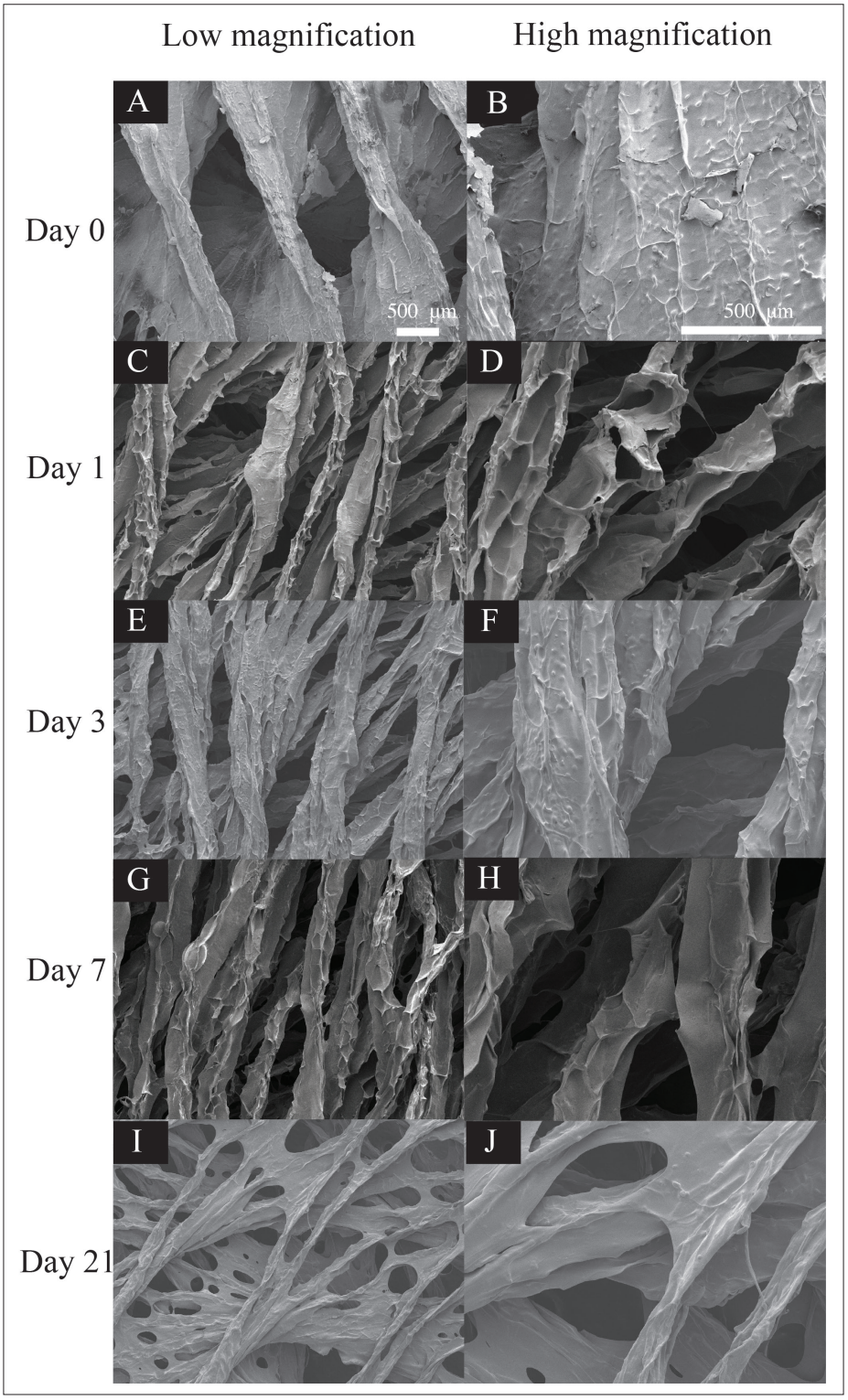

Figure 10. Field emission scanning electron microscopy images of lyophilized cell-laden constructs at different time points. Low magnification images on (A) day 0, (C) day 1, (E) day 3, (G) day 7, and (I) day 21 (scale bar: 500 µm; magnification: 30×), and corresponding higher-magnification images on (B) day 0, (D) day 1, (F) day 3, (H) day 7, and (J) day 21 (scale bar: 500 µm; magnification: 100×).

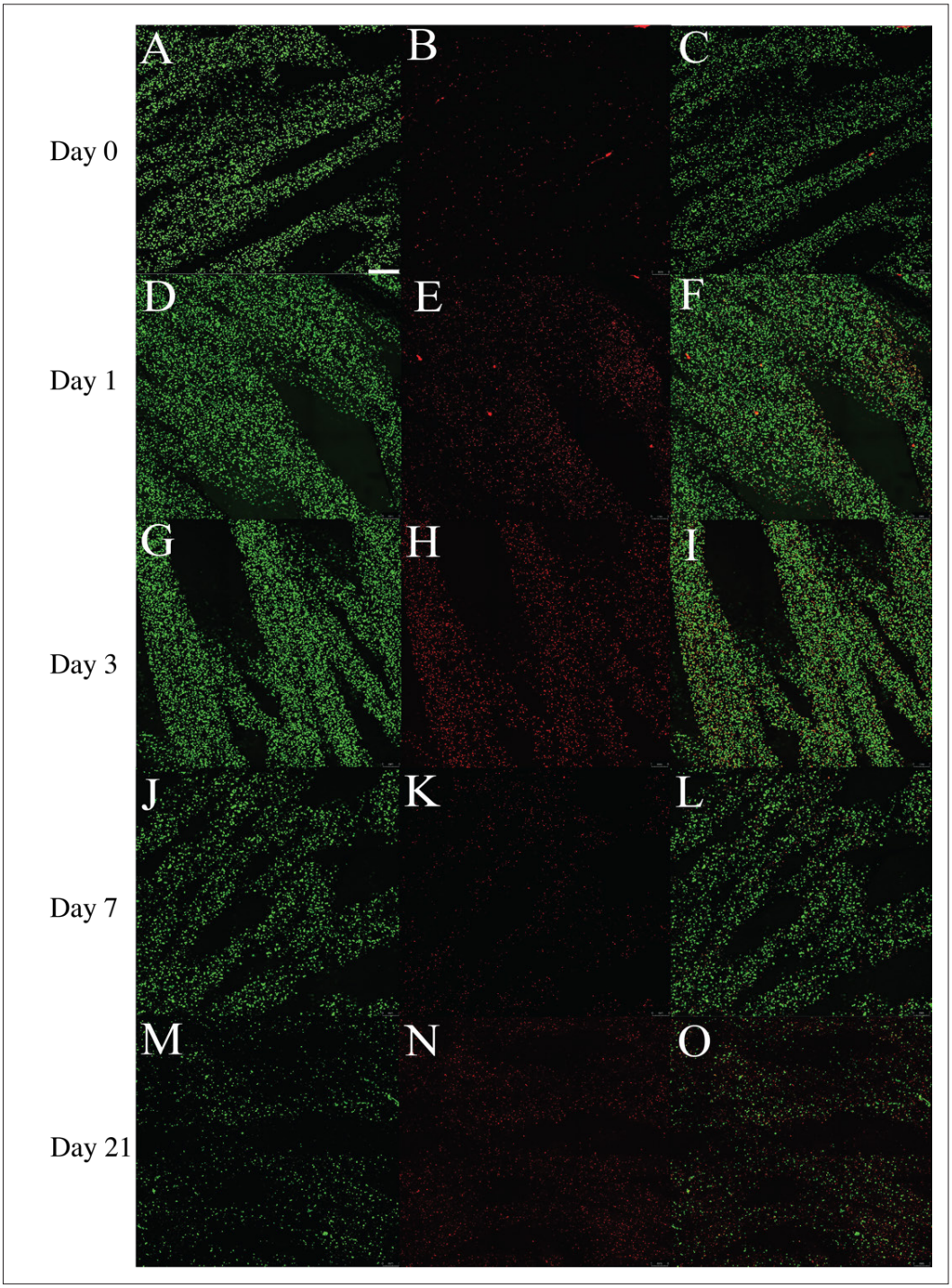

Figure 11. Cell viability assessment using the live/dead assay for three-dimensional-bioprinted constructs at different time points: (A–C) day 0, (D–F) day 1, (G–I) day 3, (J–L) day 7, and (M–O) day 21. The left column (A, D, G, J, M) displays live cells stained with calcein-AM, the middle column (B, E, H, K, N) shows dead cells stained with propidium iodide, and the right column (C, F, I, L, O) presents merged images of live and dead cells (scale bar: 500 μm; magnification: 5×).

down approach.[20] Subsequently, cell-free and cell-laden constructs were fabricated to evaluate the effect of cell presence on the physical and morphological properties of the constructs over time.

During the process of extrusion 3D-bioprinting, cells encounter various mechanical forces that can impact their viability and functionality. Among these forces, shear stress is considered particularly detrimental to cell viability and survival.[32] It is an inherent mechanical stress experienced by cells in all bioprinting approaches, posing a significant risk of cell damage and death depending on its intensity.[32] Controlling the shear forces generated within the bioprinting nozzle can enhance cell survival and proliferation post-3D-bioprinting.[33]

To minimize shear forces during 3D-bioprinting, it is essential to adjust the printing pressure to the minimum level that ensures a steady flow of bioink through the bioprinting nozzle, while also extruding the bioink at a deposition speed that closely matches the intended printing speed. Rheological studies on the bioink, including both steady shear and oscillatory shear tests, are essential for evaluating the bioink's suitability for 3D-bioprinting. These studies also provide crucial data for computational modeling of bioink flow behavior, supporting CFD simulations. CFD helps determine the appropriate pressure and printing speed, resulting in good printability and enhanced cell viability for printed constructs.

The findings of this study highlight the significant impact of cells on the viscosity of the bioink. While many studies on 3D-bioprinting have focused solely on the rheological behavior of the bioink without considering the presence of cells, our findings indicate that HUVECs can indeed have a significant effect on bioink rheology. The rheological behavior of both cell-free Alg3Gel1 and cell-laden Alg3Gel1 constructs exhibited shear-thinning behavior, which is advantageous for 3D-printing or bioprinting. This shear-thinning property is a key factor in ensuring proper printability and maintaining shape fidelity in extrusion printing.[28] The incorporation of cells increased the viscosity of the hydrogel from 21.27 to 167.95 Pa·s at a shear rate of 0.009992 s^{-1} and from 0.72 to 6.41 Pa·s at a shear rate of 999.95 s^{-1}. These findings are consistent with previous studies that indicate an increase in viscosity with higher cell densities.[34] However, these findings also contradict other studies that demonstrate a decrease in viscosity upon introducing cells or with increasing cell concentration,[35,36] suggesting a possible dependency on cell type, cell density, and hydrogel composition.

In this study, the increased viscosity of the cell-laden Alg3Gel1 construct is mostly related to the introduction of additional particulate matter in the bioink and potential interactions among the cell–hydrogel and/or cell–cell components. Because cells act as non-soluble microparticles suspended within the hydrogel, the system shifts from a single-phase to a two-phase structure.[37] This also explains the higher G' and G" of cell-laden bioink compared to cell-free Alg3Gel1. It is worth noting that the cell-laden Alg3Gel1 constructs exhibited a higher G' than G" compared to the Alg3Gel1 and Alg3 samples. This characteristic is advantageous for 3D-printing , as it ensures that the material can be extruded while maintaining its shape after extrusion.[38]

The higher viscosity of cell-laden bioink may require greater extrusion forces, leading to increased shear stresses experienced by the cells.[39] This can result in potential cell damage or even death. Therefore, based on the initial study of printability and the determination of a suitable printing pressure and speed for achieving a printable structure, a computational technique can be employed to determine the appropriate printing speed and pressure. This ensures that the difference between the defined printing velocity and the outlet velocity is minimized. Furthermore, the appropriate printing speed and pressure for producing scaffold fibers can be refined by conducting viability assays to determine the final appropriate parameters. This approach ensures high cell viability along with high printability and structural fidelity.

The rheological and mechanical properties, swelling behavior, and degradation of the structures were investigated by assessing the viscoelasticity, elastic modulus, swelling, and mass retention percentages of both cell-free and cell-laden constructs to determine the influence of living cells on these parameters. Evaluating both the elastic modulus and the viscoelastic properties (storage and loss modulus) provides a more comprehensive understanding of the mechanical behavior of the constructs. Although the static elastic modulus provides insights into the yielding strain (or stress) and the linear stress–strain response of a material, it cannot reveal the complex modulus, which encompasses both the storage (elastic) and loss (viscous) components.[40] This distinction is crucial, as no material is purely elastic or viscous. Instead, a material's behavior can range from solid-like to liquid-like depending on the frequency of the applied force. Therefore, evaluating a construct's response to dynamic stimuli is crucial in fields where frequency-dependent variations in modulus are significant.[40]

The myocardium exhibits dynamic viscoelastic behavior— its stiffness can vary depending on the speed and extent of the stretch it experiences. However, myocardial viscoelasticity often increases in myocardial

diseases, which can lead to reduced cardiac output by impeding diastolic filling.[41] Although many studies have measured the elasticity of the human heart, measuring its viscosity remains a challenge.[42] Simulations within the physiological range of the human heartbeat suggest that the viscous component of the human heart has a minor influence on its overall behavior, indicating that the human heart is hyperelastic.[42] Although both cell-free and cell-laden constructs exhibited viscoelastic behavior, the cell-laden constructs displayed more solid-like behavior at lower frequencies and more liquid-like behavior at higher frequencies, whereas the cell-free constructs exhibited the opposite trend.

The high water content in cell-laden constructs—since water accounts for 70% or more of total cell mass[43]—is most likely responsible for the more liquid-like response of the cell-laden constructs compared to the cell-free scaffolds.[44] This was confirmed by compressive mechanical tests measuring the elastic modulus of the constructs, which generally showed a lower elastic modulus for cell-laden constructs compared to cell-free scaffolds. However, only two out of the five time points showed a statistically significant difference.

Although there is limited knowledge comparing the mechanical properties of cell-free and cell-laden constructs, our findings are supported by a previous study[45] on hyaluronic acid-based constructs for cartilage tissue engineering, where the cell-laden constructs exhibited a lower elastic modulus compared to cell-free scaffolds on day 1. The mechanical properties of these constructs can vary depending on several factors, such as the specific type of cells used, the scaffold material, or the method by which the cells are incorporated into the scaffolds. For example, in a study involving smooth muscle cells, both smooth muscle cell-seeded and unseeded elastin-modified collagen sheets showed a lower Young's modulus compared to unseeded collagen sheets over 3 weeks, highlighting how different experimental conditions can influence the mechanical outcomes.[46]

A healthy myocardium has a stiffness of 10–15 kPa, while an infarcted myocardium has a stiffness of 35–70 kPa. To maintain their striations and a beating frequency of 1 Hz, cardiac myocytes should be grown on a substrate with stiffness comparable to that of a healthy myocardium. In contrast, growing cardiac cells on stiffer matrices may lead to a shorter beating period.[47,48] In this study, both cell-free and cell-laden constructs exhibited an elastic modulus of less than 15 kPa over time, indicating their potential suitability as substrates for culturing cardiac myocytes. The cell-laden constructs contain cells with high water content, which affects their viscoelastic behavior and elastic modulus. This could explain the lower swelling percentage of cell-laden constructs compared to cell-free scaffolds, although the difference is not statistically significant.

While the mass retention percentages showed a trend similar to that of the swelling percentages for cell-free scaffolds, the mass retention for cell-laden constructs demonstrated almost no mass loss. The higher mass retention in cell-laden constructs compared to cell-free scaffolds could be attributed to their lower swelling percentages, resulting in reduced hydrolytic mass loss. Additionally, the high swelling percentage of cell-free alginate-based scaffolds is likely associated with a lower content of calcium ions.[49] This relationship may be slightly altered in cell-laden constructs due to potential interactions between the cells and the calcium ions present within the construct.

However, the FESEM images of cell-laden constructs revealed significant signs of mass loss over time, similar to cell-free scaffolds. While this was anticipated for cell-free scaffolds based on the mass retention percentage, it was not expected for cell-laden constructs, which exhibited an almost 100% mass retention percentage. Interestingly, the FESEM images revealed that the cell-laden constructs exhibited more signs of mass loss until day 7, but by day 21, they exhibited a more integrated structure compared to cell-free scaffolds. This suggests that weight-based mass retention characterization may not be an appropriate method for assessing mass loss in cell-laden constructs.

Although there is limited knowledge regarding the impact of cells on the physical and mechanical properties of engineered tissues, our findings highlight the complex influence of HUVECs in these constructs. This underscores the need for further research on the mechanical properties of cell-laden engineered tissues, especially in contexts involving cell encapsulation for both *in vitro* and *in vivo* studies. Additionally, the cell viability assay exhibited high cell viability after 3D-bioprinting until day 7. The cells may have entered a resting phase after 7 days due to prolonged stationary incubation or inadequate nutrient supply, leading to cell death.[50] This suggests that the cell-laden constructs reached their maximum cellular capacity after 7 days.[50]

The primary objective of this study was to monitor cell viability following bioprinting, rather than to assess long-term proliferation or functionality. We have successfully achieved this goal, demonstrating high post-printing cell viability. Future studies aiming to develop functional vascular networks will require the incorporation of targeted treatments, such as supplementation with specific growth factors to promote vascularization, and the

assessment of long-term cellular functionality. In contrast, the present work was deliberately focused on preserving viable cells during and after printing and on examining how their presence affects the mechanical, rheological, and microstructural properties of the scaffolds.

5. Conclusion

Developing 3D-bioprinted tissue constructs offers promising opportunities for replicating complex, tissue-like structures. However, key challenges persist, particularly in maintaining high cell viability during printing and in understanding how living cells influence the mechanical and physical properties of the constructs. To address these challenges, we incorporated HUVECs into alginate–gelatin hydrogels and bioprinted them under optimized conditions, focusing on minimizing printing pressure-induced cell damage and elucidating the effects of incorporated cells.

The mechanical and rheological properties of both cell-free and cell-laden constructs were evaluated to assess the long-term influence of cells on these properties. Key findings revealed that cell-laden constructs exhibited higher viscosity and a greater storage modulus than the loss modulus compared to cell-free constructs. Based on preliminary cell viability data, CFD modeling, and experimental observations, 25 kPa was identified as the appropriate pressure for bioprinting these constructs. This pressure minimizes process-induced forces on the cells while maintaining a steady bioink flow through the nozzle, thereby reducing strand deformation and cell stretching during deposition.

Although both cell-laden and cell-free constructs exhibited viscoelastic behavior, the cell-laden constructs displayed more fluid-like characteristics, as evidenced by a lower elastic modulus relative to cell-free scaffolds. The cell-free scaffolds also exhibited a higher swelling percentage than the cell-laden constructs. While mass retention assays suggested minimal degradation over time, FESEM imaging revealed distinct signs of degradation in cell-free constructs. Furthermore, high cell viability was maintained in the 3D-bioprinted constructs for at least 7 days post-printing.

Our findings demonstrate the potential of cell-laden constructs with an angular design mimicking the orientation of heart myofibrils as suitable substrates for cardiomyocyte growth, particularly following vascularization within the constructs. As the present study primarily focused on maintaining cell viability post-printing rather than assessing cellular functionality, future research should investigate the functional behavior of incorporated endothelial cells, with the aim of promoting vascularization to support cardiomyocyte integration and maturation in these bioprinted constructs.

Acknowledgments

The authors express their gratitude to Dr. Graham George and Dr. Ingrid J. Pickering for generously providing access to the confocal microscope. Special thanks are also extended to Peyman Asadi for designing the graphical abstract.

Funding

This study was supported by the Natural Sciences and Engineering Research Council of Canada (grant number: PGPIN 06396-2019). Additional support was provided through the Saskatchewan Research Chair in Clinical Stroke Research, awarded to MK by the Heart and Stroke Foundation, the Saskatchewan Health Research Foundation, and the University of Saskatchewan College of Medicine. The study was further supported by a Dean's Scholarship and a Biomedical Engineering Devolved Scholarship, both awarded to FK by the University of Saskatchewan.

Conflict of interest

Xiongbiao Chen serves as the Editorial Board Member of the journal, but did not in any way involve in the editorial and peer-review process conducted for this paper, directly or indirectly. Other authors declare they have no competing interests.

Author contributions

Conceptualization: Farinaz Ketabat, Michael E. Kelly, Ildiko Badea, Xiongbiao Chen
Data curation: Farinaz Ketabat
Formal analysis: Farinaz Ketabat, Reza Gharraei, Alex Guinle
Funding acquisition: Michael E. Kelly, Ildiko Badea, Xiongbiao Chen
Investigation: Farinaz Ketabat, Reza Gharraei, Alex Guinle, Nicole J. Sylvain
Methodology: Farinaz Ketabat, Reza Gharraei, Alex Guinle
Resources: Michael E. Kelly, Ildiko Badea, Xiongbiao Chen
Supervision: Michael E. Kelly, Ildiko Badea, Xiongbiao Chen
Writing – original draft: Farinaz Ketabat
Writing – review & editing: All authors

Ethics approval and consent to participate

Not applicable.

Consent for publication

Not applicable.

Availability of data

Data is available from the corresponding author upon reasonable request.

Further disclosure

This work was previously presented at the 2024 CSPS/CCCRS Annual Symposium (June 10–13, 2024, Edmonton, Alberta, Canada) as a poster. During the preparation of this work, FK used ChatGPT 4.0 and Copilot in order to improve language and readability. After using this tool/service, FK reviewed and edited the content as needed and takes full responsibility for the content of the publication.

References

1. Cho S, Discher DE, Leong KW, Vunjak-Novakovic G, Wu JC. Challenges and opportunities for the next generation of cardiovascular tissue engineering. *Nat Methods*. 2022;19(9):1064-1071. doi: 10.1038/s41592-022-01591-3
2. Garbern JC, Lee RT. Heart regeneration: 20 years of progress and renewed optimism. *Dev Cell*. 2022;57(4):424-439. doi: 10.1016/j.devcel.2022.01.012
3. Izadifar M, Chapman D, Babyn P, Chen X, Kelly ME. UV-assisted 3D-bioprinting of nanoreinforced hybrid cardiac patch for myocardial tissue engineering. *Tissue Eng Part C Methods*. 2018;24(2):74-88. doi: 10.1089/ten.tec.2017.0346
4. Sobanski PZ, Alt-Epping B, Currow DC, *et al*. Palliative care for people living with heart failure: European Association for Palliative Care Task Force expert position statement. *Cardiovasc Res*. 2020;116(1):12-27. doi: 10.1093/cvr/cvz200
5. Truby LK, Rogers JG. Advanced heart failure: epidemiology, diagnosis, and therapeutic approaches. *Heart Fail*. 2020;8(7):523-536. doi: 10.1016/j.jchf.2020.01.014
6. Tenreiro MF, Louro AF, Alves PM, Serra M. Next generation of heart regenerative therapies: progress and promise of cardiac tissue engineering. *NPJ Regen Med*. 2021;6(1):30. doi: 10.1038/s41536-021-00140-4
7. Wang Z, Wang L, Li T, *et al*. 3D-bioprinting in cardiac tissue engineering. *Theranostics*. 2021;11(16):7948. doi: 10.7150/thno.61621
8. Liu N, Ye X, Yao B, *et al*. Advances in 3D-bioprinting technology for cardiac tissue engineering and regeneration. *Bioact Mater*. 2021;6(5):1388-1401. doi: 10.1016/j.bioactmat.2020.10.021
9. Agarwal T, Fortunato GM, Hann SY, *et al*. Recent advances in bioprinting technologies for engineering cardiac tissue. *Mater Sci Eng C*. 2021;124:112057. doi: 10.1016/j.msec.2021.112057
10. Chang YC, Mirhaidari G, Kelly J, Breuer C. Current challenges and solutions to tissue engineering of large-scale cardiac constructs. *Curr Cardiol Rep*. 2021;5(47):1-6. doi: 10.1007/s11886-021-01474-7
11. Ning L, Betancourt N, Schreyer DJ, Chen X. Characterization of cell damage and proliferative ability during and after bioprinting. *ACS Biomater Sci Eng*. 2018;4(11):3906-3918. doi: 10.1021/acsbiomaterials.8b00714
12. Noroozi R, Arif ZU, Taghvaei H, *et al*. 3D and 4D bioprinting technologies: a game changer for the biomedical sector? *Ann Biomed Eng*. 2023;51(8):1683-1712. doi: 10.1007/s10439-023-03243-9
13. Tiruvannamalai-Annamalai R, Armant DR, Matthew HWT. A glycosaminoglycan based, modular tissue scaffold system for rapid assembly of perfusable, high cell density, engineered tissues. *PLoS One*. 2014;9(1):e84287. doi: 10.1371/journal.pone.0084287
14. Ketabat F, Alcorn J, Kelly ME, Badea I, Chen X. Cardiac tissue engineering: a journey from scaffold fabrication to in vitro characterization. *Small Sci*. 2024;4(9):2400079. doi: 10.1002/smsc.202400079
15. Chen XB, Anvari-Yazdi AF, Duan X, *et al*. Biomaterials/bioinks and extrusion bioprinting. *Bioact Mater*. 2023;28:511-536. doi: 10.1016/j.bioactmat.2023.06.006
16. Ning L, Chen X. A brief review of extrusion-based tissue scaffold bio-printing. *Biotechnol J*. 2017;12(8):1600671. doi: 10.1002/biot.201600671
17. Lemarié L, Anandan A, Petiot E, Marquette C, Courtial EJ. Rheology, simulation and data analysis toward bioprinting cell viability awareness. *Bioprinting*. 2021;21:e00119. doi: 10.1016/j.bprint.2020.e00119
18. Krishnamoorthy S, Noorani B, Xu C. Effects of encapsulated cells on the physical–mechanical properties and microstructure of gelatin methacrylate hydrogels. *Int J Mol Sci*. 2019;20(20):5061. doi: 10.3390/ijms20205061
19. Otto IA, Levato R, Webb WR, *et al*. Progenitor cells in auricular cartilage demonstrate cartilage-forming capacity in 3D hydrogel culture. *Eur Cell Mater*. 2018;35:132. doi: 10.22203/eCM.v035a10
20. Ketabat F, Maris T, Duan X, *et al*. Optimization of 3D-printing and in vitro characterization of alginate/gelatin lattice and angular scaffolds for potential cardiac tissue engineering. *Front Bioeng Biotechnol*. 2023;11:1161804. doi: 10.3389/fbioe.2023.1161804
21. Maiullari F, Costantini M, Milan M, *et al*. A multi-cellular 3D-bioprinting approach for vascularized heart tissue engineering based on HUVECs and iPSC-derived cardiomyocytes. *Sci Rep*. 2018;8(1):13532. doi: 10.1038/s41598-018-31848-x

22. Sánchez-Sánchez R, Rodríguez-Rego JM, Macías-García A, Mendoza-Cerezo L, Díaz-Parralejo A. Relationship between shear-thinning rheological properties of bioinks and bioprinting parameters. *Int J Bioprint*. 2023;9(2):687. doi: 10.18063/ijb.687

23. Frank MW. *Viscous Fluid Flow. International Edition, 2nd ed. New York, NY: McGraw-Hill;* 1991.

24. Vey E, Rodger C, Booth J, Claybourn M, Miller AF, Saiani A. Degradation kinetics of poly (lactic-co-glycolic) acid block copolymer cast films in phosphate buffer solution as revealed by infrared and Raman spectroscopies. *Polym Degrad Stab*. 2011;96(10):1882-1889. doi: 10.1016/j.polymdegradstab.2011.07.011

25. Cross MM. Rheology of non-Newtonian fluids: a new flow equation for pseudoplastic systems. *J Colloid Sci*. 1965;20(5):417-437. doi: 10.1016/0095-8522(65)90022-X

26. Chen DXB. *Extrusion Bioprinting of Scaffolds for Tissue Engineering*. 2nd ed. Cham, Switzerland: Springer International Publishing AG; 2025. doi: 10.1007/978-3-031-72471-8

27. Bercea M. Rheology as a tool for fine-tuning the properties of printable bioinspired gels. *Molecules*. 2023;28(6):2766. doi: 10.3390/molecules28062766

28. Bom S, Ribeiro R, Ribeiro HM, Santos C, Marto J. On the progress of hydrogel-based 3D-printing: Correlating rheological properties with printing behaviour. *Int J Pharm*. 2022;615:121506. doi: 10.1016/j.ijpharm.2022.121506

29. Habib, M. A., Khoda, B. Rheological analysis of bio-ink for 3D-bio-printing processes. *J Manuf Process*. 2022;76:708–718. doi: 10.1016/j.jmapro.2022.02.048

30. Chopin-Doroteo M, Mandujano-Tinoco EA, Krötzsch E. Tailoring of the rheological properties of bioinks to improve bioprinting and bioassembly for tissue replacement. *Biochim Biophys Acta Gen Subj*. 2021;1865(2):129782. doi: 10.1016/j.bbagen.2020.129782

31. Ning L, Gil CJ, Hwang B, *et al*. Biomechanical factors in three-dimensional tissue bioprinting. *Appl Phys Rev*. 2020;7(4):041319. doi: 10.1063/5.0023206

32. Boularaoui S, Al Hussein G, Khan KA, Christoforou N, Stefanini C. An overview of extrusion-based bioprinting with a focus on induced shear stress and its effect on cell viability. *Bioprinting*. 2020;20:e00093. doi: 10.1016/j.bprint.2020.e00093

33. Persaud A, Maus A, Strait L, Zhu D. 3D-bioprinting with live cells. *Eng Regen*. 2022;3(3):292-309. doi: 10.1016/j.engreg.2022.07.002

34. Diamantides N, Dugopolski C, Blahut E, Kennedy S, Bonassar LJ. High density cell seeding affects the rheology and printability of collagen bioinks. *Biofabrication*. 2019;11(4):045016. doi: 10.1088/1758-5090/ab3524

35. Majumder N, Mishra A, Ghosh S. Effect of varying cell densities on the rheological properties of the bioink. *Bioprinting*. 2022;28:e00241. doi: 10.1016/j.bprint.2022.e00241

36. Ouyang L, Yao R, Zhao Y, Sun W. Effect of bioink properties on printability and cell viability for 3D bioplotting of embryonic stem cells. *Biofabrication*. 2016; 8(3):035020. doi: 10.1088/1758-5090/8/3/035020

37. Chen DXB. Preparation of Scaffold solutions and characterization of their flow behavior. In: *Extrusion Bioprinting of Scaffolds for Tissue Engineering Applications*. Cham, Switzerland: Springer; 2019:91-115. doi: 10.1007/978-3-030-03460-3_5

38. Kimbell G, Azad MA. Chapter fifteen — 3D-printing: bioinspired materials for drug delivery. In: Nurunnabi M, ed. *Bioinspired and Biomimetic Materials for Drug Delivery*. Woodhead Publishing Series in Biomaterials. Cambridge, UK: Woodhead Publishing; 2021: 295-318. doi: 10.1016/B978-0-12-821352-0.00011-3

39. Gao T, Gillispie GJ, Copus JS, *et al*. Optimization of gelatin–alginate composite bioink printability using rheological parameters: a systematic approach. *Biofabrication*. 2018;10(3):034106. doi: 10.1088/1758-5090/aacdc7

40. Patra S, Ajayan PM, Narayanan TN. Dynamic mechanical analysis in materials science: the Novice's Tale. *Oxf Open Mater Sci*. 2021;1(1):itaa001. doi: 10.1093/oxfmat/itaa001

41. Caporizzo MA, Prosser BL. Need for speed: the importance of physiological strain rates in determining myocardial stiffness. *Front Physiol*. 2021;12:696694. doi: 10.3389/fphys.2021.696694

42. Tikenoğulları OZ, Costabal FS, Yao J, Marsden A, Kuhl E. How viscous is the beating heart? Insights from a computational study. *Comput Mech*. 2022;70(3):565-579. doi: 10.1007/s00466-022-02180-z

43. Wang Z, St-Onge MP, Lecumberri B, *et al*. Body cell mass: model development and validation at the cellular level of body composition. *Am J Physiol Endocrinol Metab*. 2004;286(1):E123-E128. doi: 10.1152/ajpendo.00227.2003

44. Hasan A, Ragaert K, Swieszkowski W, *et al*. Biomechanical properties of native and tissue engineered heart valve constructs. *J Biomech*. 2014;47(9):1949-1963. doi: 10.1016/j.jbiomech.2013.09.023

45. Levett PA, Hutmacher DW, Malda J, Klein TJ. Hyaluronic acid enhances the mechanical properties of tissue-

engineered cartilage constructs. *PLoS One*. 2014; 9(12):e113216.
doi: 10.1371/journal.pone.0113216

46. Ghazanfari S, Alberti KA, Xu Q, Khademhosseini A. Evaluation of an elastic decellularized tendon-derived scaffold for the vascular tissue engineering application. *J Biomed Mater Res A*. 2019;107(6):1225-1234.
doi: 10.1002/jbm.a.36622

47. Janmey, P. A., Miller, R. T. Mechanisms of mechanical signaling in development and disease. *J Cell Sci*. 2011;124(1):9-18.
doi: 10.1242/jcs.071001

48. Engler AJ, Carag-Krieger C, Johnson CP, *et al*. Embryonic cardiomyocytes beat best on a matrix with heart-like elasticity: scar-like rigidity inhibits beating. *J Cell Sci*. 2008;121(22):3794-3802.
doi: 10.1242/jcs.029678

49. Moreno-Castellanos N, Velásquez-Rincón MC, Rodríguez-Sanabria AV, Cuartas-Gómez E, Vargas-Ceballos O. Encapsulation of beta-pancreatic cells in a hydrogel based on alginate and graphene oxide with high potential application in the diabetes treatment. *J Mater Res*. 2023;38(10):2823-2837.
doi: 10.1557/s43578-023-01009-6

50. Mohammadrezaei D, Moghimi N, Vandvajdi S, Powathil G, Hamis S, Kohandel M. Predicting and elucidating the post-printing behavior of 3D-printed cancer cells in hydrogel structures by integrating in-vitro and in-silico experiments. *Sci Rep*. 2023;13(1):1211.
doi: 10.1038/s41598-023-28286-9